Title: Solar flare X-ray impacts on long subionospheric VLF paths

Authors:

Samuel R. G. Belcher[1], Mark A. Clilverd[2], Craig J. Rodger[1], Sophie Cook[1], Neil R. Thomson[1], James B. Brundell[1], Tero Raita[3]

[1]Physics Dept., University of Otago, Dunedin, New Zealand.

[2]British Antarctic Survey (UKRI-NERC), Cambridge, United Kingdom.

[3]Sodankylä Geophysical Observatory, University of Oulu, Sodankylä, Finland.

Plain Language Summary

In this work previous analysis of solar flare impacts on the propagation of radiowaves beneath the Earth's ionosphere is extended. These space weather effects can cause disruptions to aviation navigation and communications systems, affecting flight routing and causing passenger delays. Perturbations of signals coming from man-made communication transmitters in the very low frequency range are used to measure solar flare X-ray flux levels over a wider range of event sizes than done previously. We have shown that the accuracy of the determined flare size is dependent on the distance between the transmitter and the measuring receiver, with longer paths being better. Using only ground-based measurements to estimate the flare size is a reasonable proxy for satellite X-ray data, suggesting a technique for an independent solar flare monitoring capability.

Main point #1: Ground-based subionospheric VLF phase measurements of M- and X-class flare impacts are analysed on N-S and W-E propagation paths

Main point #2: Good agreement is found between the peak XL flux derived using VLF phase for M- and X- class flares and those measured by GOES

Main point #3: Regression analysis on the two paths shows the flux uncertainties increase in inverse proportion to the transmitter to receiver path length

Abstract

Solar flares increase the electron number concentration in the day-time ionosphere, potentially affecting radiowave propagation over several frequency ranges. In this study, we use ionospheric observations to determine both peak magnitudes and time variations of solar flare X-rays without using the direct measurement from the flare.. Ground-based observations of VLF transmitter phase perturbations are compared against measured X-ray flux levels during solar flares. Flare fluxes derived here from VLF phases on a west-east subionospheric path are compared with those from a previously analyzed north-south path. Using a wider selection of solar flares, including M-class flares for the first time, the best fit equations and root mean square (RMS) errors are computed with improved standard deviation (SD) uncertainty estimates for the peak fluxes. Good agreement is found between peak long X-ray wavelength fluxes (XL, 0.1-0.8 nm) derived for M- and X- class flares and those measured by the GOES satellites. Linear regression analysis on the two paths shows the uncertainties increase in inverse proportion to the path length. Investigations were made with a limited set of 'operational' parameters that could be used to derive XL fluxes. No

increases in RMS or SD uncertainty levels were introduced by the removal of satellite-based regression parameters such as, the XL flux level measured prior to the flare onset. As such, these techniques support the idea of nowcasting M- and X-class flares from entirely ground-based measurements.

1. Introduction

The D-region is the lowest layer of the ionosphere, extending from about 60 km to 95 km altitude during day time solar illumination conditions. The region has complex chemical reactions and multiple sources of ionisation [e.g., Hargreaves, pg 229, 1992]. Solar Lyman alpha radiation (121.6 nm) is the dominant ionisation mechanism responsible for the generation of the day-time D-region. However, other sources such as X-rays, EUV, UV, and galactic cosmic rays are significant at various altitudes throughout the D-region depending on their energy [Rodger et al., 2007; Thomson et al., 2021 and references therein]. Solar flares increase the electron concentration in the day-time D-region due to a significant increase in X-ray flux ionising N_2 and O_2 [Mitra, pg170, 1974]. The ionisation due to both Lyman-alpha and X-rays is dependent on the Solar Zenith Angle (SZA), with ionisation rates decreasing with larger SZA. Changes in the D-region can affect radiowave propagation over several frequency bands of interest to this study, including Very Low Frequency (VLF, 3-30 kHz), High Frequency (HF, 3-30MHz), and Very High Frequency (VHF, 30-300MHz).

Airlines use a combination of line-of-sight VHF and HF radiowaves to communicate between aircraft and control towers [Cannon et al., 2013]. Long-distance, i.e., trans-oceanic flights rely on HF communications to provide continuous information exchange throughout the flights. During a large solar flare HF transmissions can be significantly degraded for several hours by fading and/or noise, sometimes to the point of a blackout [Redmon et al., 2018]. Disturbances can also extend to VHF communications [ICAO, section 2.4.2, 2018]. As a result of degraded radiowave propagation during large solar flares, flights may need to be rerouted and/or rescheduled depending on the severity of the impact on communication and navigation systems. For this reason, the International Civil Aviation Organization has identified up-to-date information on space weather as a new operational requirement [ICAO, section 1.4.3, 2018].

There is a growing list of case studies demonstrating solar flare impacts on aviation and maritime navigation [e.g., Knipp et al. 2016; Berdermann et al., 2018; Redmon et al., 2018; Marqué et al., 2018; Sato et al., 2019]. An updated Safety Information Bulletin regarding the effects of space weather on aviation lists radio blackouts, fading, and diminished reception on HF and VHF communications as a consequence of solar flares [EASA, 2021]. The bulletin recommends that solar weather forecasts and nowcasts be used for inflight situational awareness, and flight management. As of late November 2019, operational global space weather forecasts are being provided for civil aviation [Knipp and Hapgood, 2019]. As a result of these activities there is renewed interest in the impact of solar flares on ground-based VLF transmitter signals and the determination of solar X-ray flux levels from the observed perturbations [e.g. George et al., 2019].

Previous work has shown that VLF radiowaves can be used to investigate the D-region impacts of solar flares [e.g., Mitra, 1974; McRae and Thomson, 2004; Thomson et al., 2004; Thomson et al., 2005; Žigman et al., 2007; Kolarski and Grubor, 2014; Wenzel et al., 2016]. Recently, George et al. [2019] investigated the comparative usefulness of VLF amplitude and phase measurements as an accurate measure of solar flare X-ray flux. Narrow-band radiowaves received from the transmitter with call sign NPM in Hawaii by a VLF receiver located at Scott Base, Antarctica were analysed. A small number of X-class flares were considered. To determine a relationship between X-ray flux and VLF perturbation levels, linear regression was performed between the short and long (XS, 0.05-0.4 nm, and XL, 0.1-0.8 nm, respectively) X-ray wavelengths, VLF perturbation level, and SZA. The best result was achieved using phase perturbation data to determine X-ray flux levels in the XL range. Figure 1 shows a schematic that illustrates the systems impacted by solar flare effects in the ionospheric D-region, namely VLF subionospheric signal propagation, along with aviation radar systems and air-traffic control (ATC) communication systems..

This study builds on the results of George et al. [2019] in order to identify a technique that is applicable to a wider range of VLF propagation paths. Using VLF phase measurements flare X-ray peak flux estimates on a west-east (W-E) orientated path are compared with the previously analysed north-south (N-S) orientated path. Using a wider selection of solar flares, which includes M-class flares for the first time, the George et al. analysis for the same N-S path, NPM to Scott Base is extended. The best fit equations and root mean square (RMS) errors are computed with improved standard deviation (SD) uncertainty estimates of the peak fluxes. Analysis is then applied to flare-induced phase perturbations on a long W-E path across the North Atlantic, and a comparison of the suitability of such paths for X-ray flux determination is made. Finally, a technique that uses the VLF phase data to identify the flare start time is evaluated thus providing an independent verification of the solar flare X-ray flux (and flare class) without the use of any satellite X-ray flux parameters. This work extends the framework put forward by George et al. [2019] to provide fully-ground based measurments of the X-ray flux levels associated with large solar flares.

2. Experimental details

2.1 VLF datasets used

Two separate VLF paths are considered, both of which are part of the Antarctic-Arctic Radiation-belt (Dynamic) Deposition - VLF Atmospheric Research Konsortium (AARDDVARK) [Clilverd et al, 2009]. The largely N-S orientated path from the NPM transmitter operating at 21.4 kHz in Hawaii, received at Scott Base, Antarctica is described in George et al. [2019]. The path length is 11,246 km. VLF amplitude and phase observations averaged to five seconds time resolution from January 2009 until June 2018 are analysed for solar flare-induced perturbations, although large flare perturbations primarily occurred during 2011-2015. In the current study we extend our analysis to a West-East orientated path across the North Atlantic. These are similar VLF amplitude and phase observations from 2010 until 2019, also averaged to 5 s time resolution. M- and X-class flares analysed on this path were limited to 2011-2015, with one additional M-class flare in 2017. The path runs from the mid-latitude NAA transmitter operating at 24.0 kHz in Cutler, Maine, USA to Sodankylä Geophysical Observatory (SGO) in Lapland, Finland, over a distance of 5667 km. A description of the NAA-SGO data collection details can be found in Clilverd et al. [2010] and Neal et al. [2015]. Both VLF receivers are UltraMSK software defined radio systems connected to magnetic field sensing loops. Figure 2 shows a map of both paths.

Apart from the different orientations of the two paths there are some similarities, namely that both are predominately all-sea paths, and the transmitter frequencies are separated by only 2.6 kHz (~12%). These similarities suggest that the modal make-up of the radiowaves along the path from transmitter towards the receiver should be similar, and the phase perturbation response to solar flare X-ray flux enhancements should be comparable [Thomson et al., 2005]. Lotz and Clilverd [2019] related solar-flare peak flux values to phase perturbation levels on two different paths by expressing the relative path lengths in terms of a wavelength ratio. The idea was also considered in George et al. [2019]. In the current study, the wavelength ratio of the NPM-Scott Base path relative to the NAA-SGO path is 1.8, whilst the ratio of the path lengths in km is 2.0. For this study we contrast the results relating to the two different paths in terms of geographical path length alone because of the similarity of the frequencies transmitted.

2.2 Solar zenith angle selection of flares

The flare-induced phase perturbation effects on paths of different lengths, and with different local time ranges along the paths, can be best compared when the whole path is illuminated during each solar flare. In order to determine if the VLF path was illuminated when a solar flare occurred the SZA was calculated using the Solar Geometry 2 (SG2) algorithm [Blanc and Wald, 2012]. The altitude was set to the altitude of the lower D-region daytime reflection height, i.e., 65 km, and generated without atmospheric corrections.

Flares impacting either of our two propagation paths were identified as having a fully illuminated VLF path if the SZA at the transmitter, the midpoint, and the receiver were all less than 80º. This limit was adopted in order to avoid periods of rapidly changing phase which occur near sunrise/sunset transitions [McRae & Thomson, 2000; Clilverd et al., 2017, 2020]. This criterion was applied throughout the duration of the flare. Flares with either missing X-ray data or VLF phase data were not included in the analysis. These selection criteria resulted in 98 M-class flares, and 6 X-class flares on the N-S NPM to Scott Base path that could be included in the analysis. A total of 3 X-class flares and 38 M-class flares met these criteria for flares occurring in the W-E orientated NAA to SGO path. Note that these numbers are considerably smaller than for the N-S path, despite a slightly longer dataset being considered for the W-E path. This is due to the nature of the long W-E path, where it is much rarer for all three of the transmitter, mid-point, and receiver, to all meet our fully illuminated condition. Note that while the condition for including a flare requires the SZA restriction to be met at the three locations, the SZA used in the following regression analysis was taken from only the mid-point of the path (following George et al. [2019]). A full listing of the solar X-ray flares analysed in the study, including flare onset times, NOAA flare classification, and SZA information, is provided as supplementary information for the NPM-Scott Base VLF data set (Table S1) and the NAA-Sodankyla VLF dataset (Table S2).

2.3 Solar Flare start and end times

NOAA currently uses an algorithm to determine the start time of solar flares [https://www.ngdc.noaa.gov/stp/solar/solarflares.html] which are given with 1 minute time resolution. The algorithm requires the X-ray flux to exceed B1.0 flare magnitude, increase continuously for 4 minutes and be greater than 1.4 times the initial value after 4 minutes [Veronig et al., 2002]. Following the method adopted in George et al. [2019] the high time resolution (~2 second) data of the GOES X-ray dataset was re-analysed. This was used to provide more precise flare start times to better compare with the 5 s resolution VLF data, while still following the same detection algorithm as NOAA. However, to provide some resilience against temporarily decreasing flux measured at the higher time resolution, times were re-assessed if the X-ray flux decreased after the initial start time. For slowly rising flare events the decreasing flux test can result in re-assessed start times that are substantially delayed relative to the original start times. On average the higher time resolution NOAA start times were identified to be about 130 s later than the 1 minute time resolution start times. In this study the more precise time is referred to as the 'NOAA start time'.

It is also possible to identify the start time of a solar flare using the VLF phase data itself, independent of the satellite observations. A similar NOAA-based algorithm was applied with a few specific modifications made in order for it to work with the VLF phase measurements. This sort of approach was attempted by George et al. [2019] but that work strictly adopted the 1.4 times criteria in the same way as the NOAA-based algorithm. However, in this study a threshold approach is applied that is expected to provide a more reliable start time estimate - particularly for weaker M-class flares. For the NPM-Scott Base flares, a threshold of 8º phase increase was adopted. For the NAA-SGO path, the threshold was 4º due to the path being roughly half the length of the NPM-Scott Base path.

For both VLF paths, there were flares that had start times much later than the NOAA based start times, mostly due to the absence of clear triggering perturbations in the phase data around the time of the start of the flare as identified by the NOAA algorithm. This is probably due to solar flux enhancements being initiated from very low starting levels of X-ray flux, which did not initially affect VLF propagation enough to cause a detectable phase perturbation on the paths studied. On average, phase-based flare start times were delayed by 56 s on the NPM-Scott Base path, and 177 s on the NAA-SGO path, relative to the high time resolution NOAA start time. However, individual flare events showed substantial deviations from the average delay value.

The end time of each flare was determined using the same format as the current NOAA definition, i.e., when the X-ray flux (or phase perturbation) has decreased by a factor of 2 from the peak level.

2.4 Linear regression analysis

Linear regression analysis is used to determine the best fit of parameters that can be used to describe the time variation of X-ray flux during a solar flare. The parameters analysed here are the same as those identified by George et al. [2019] based on previous work undertaken by Thomson et al. [2005] and Cresswell-Moorcock et al. [2015]. The linear regression between the log of the X-ray XL flux (I_L) and the VLF phase perturbation parameter ($\Delta\varphi$), includes several other parameters. These are solar zenith angle at the mid-point of the VLF path, the log of the previous day's F10.7 cm flux, and the log of the initial GOES XL X-ray flux level 5 minutes prior to the identified flare start time (denoted here by IL_5). We note here that the F10.7 flux values are expressed in SI units (SFU × 10^{-22}).The phase perturbation is measured in degrees of phase change from a zero degree starting point set at the flare start time. A full description of these parameters is given in George et al. [2019]. Section 3 of that paper discussed the use of a 5 minute delay between IL_5 and the flare start time. They found only small changes in regression results when varying the delay range over 2-10 minutes, noting that 5 minutes represented a reasonable delay time in which to obtain X-ray flux from the GOES satellites. Equation (1) in section 3.1 shows how the parameters are combined. Note that for the fully ground-based approach described in section 4, the X-ray flux level 5 minutes prior to the flare start time, IL_5, is not used. The general form of the linear regression equation between the log of the X-ray XL flux (I_L) and the VLF phase perturbation parameter ($\Delta\varphi$) is shown below:

$$Log10(I_L) = \mathrm{A}\Delta\varphi \; + \mathrm{B}\,log10(F10.7) + \mathrm{C}\,cos(SZA) \; + \mathrm{D}\,cos^2(SZA) + \mathrm{E}\,log10(IL_5) + \mathrm{constant}$$

2.5 Calculating Uncertainties

Uncertainties between the NOAA XL X-ray flux and the phase-inferred XL X-ray flux were calculated in two different ways. The uncertainty in describing the time variation of the overall flare flux was calculated using data from the start to the end of the flare as determined using the NOAA start and end times. The uncertainty in the phase-inferred magnitude of the XL X-ray flux levels at the peak of each flare was also determined.

In order to provide a direct comparison between the error analysis undertaken by George et al. [2019], a mean square error (MSE) was calculated for each flare from start to finish, using the regression equations described there. The difference between the $\log_{10}$ of the predicted X-ray flux and the $\log_{10}$ of the observed X-ray flux was found. A mean square error of 0 indicates a perfect fit between the observed and inferred fluxes. The MSE is expressed in units of flux squared. However, a more useful measure of error in terms of being described in X-ray flux units is the root mean square error (RMS), i.e., simply the square root of the MSE. Smaller RMS values indicate a better quality of the fit. In this work RMS uncertainty values are reported for the regression analysis equations developed, and express the George et al. [2019] MSE value in RMS terms in order to provide a comparison of the earlier work with the results presented here.

The uncertainty of the peak magnitude of the phase-inferred flare flux levels was determined using the standard deviation (SD, $\log_{10}(\mathrm{Wm}^{-2})$) of the difference in the $\log_{10}$ of the peak X-ray flux calculated using the regression coefficients, and the $\log_{10}$ of the NOAA/GOES-observed peak X-ray flux. This technique of determining the uncertainty of the phase-inferred peak flux through standard deviation is an improvement on the relatively simplistic maximum-difference error estimate made in George et al. [2019].

3 Results

3.1 NPM-Scott Base [using revised NOAA flare start times]

An example of the VLF data analysed for solar flare-driven perturbations is shown in Figure 3. The plot shows the phase and amplitude variations from NPM – Scott Base in three different panels. The upper panel compares the time variations of the XL X-ray flux (blue line) on 22-23 December 2015 with the NPM phase (orange line). A large enhancement of X-ray flux can be seen during the 24-hour period of the plot, when an M-class flare (flux $>10^{-5}$ Wm^{-2}) peaks at 0040 UT, 23 Dec 2015. During the flare event the VLF phase shows a clear increase from pre-flare levels, rapidly rising to a peak, with values then gradually subsiding over the subsequent hours. The time of the start of the flare is indicated by a vertical black line (in all three panels), determined by the NOAA algorithm applied to 5 s resolution X-ray data as discussed in subsection 2.3. The middle panel shows ~40 minutes of NPM phase data (red line) and XL flux (blue line) focussed around the time of the M-class flare. The lower panel shows the same period but with NPM amplitude plotted instead of phase. The larger short-term variability of the amplitude signal compared to the phase signal is probably due to high-latitude, small-scale, ionospheric D-region features [e.g., Thomson et al., 2021]. In this example event both phase and amplitude variations follow the XL flux variations during the flare event, although George et al. [2019] showed that statistically the use of amplitude measurements is less accurate than using phase as the relationships are not very consistent from event to event, leading to high uncertainties.

Previous empirical analysis of flare-driven perturbations on the NPM – Scott Base path has been limited to X-class flares [George et al., 2019]. These represent the most extreme flare flux levels, and consequently induce large, relatively easy to measure phase perturbations. In this analysis the comparison is expanded by also including weaker M-class flares. This development has the advantage of increasing the number of flare events to study, but many of the added events exhibit considerably smaller phase perturbation levels (as expected [Thomson et al., 2005]), leading to potential decreases in the accuracy of the regression fits.

The linear regression coefficient results are shown in Table 1. Coefficients shown in the table are provided for several flare datasets, each of which will be discussed in detail in the following sections of this paper and are provided as supplementary information. The regression analysis parameter coefficients for X and M-class flares on the N-S NPM to Scott Base path produce the following relationship:

$$Log10(I_L) = 6.7 \times 10^{-3}\Delta\varphi \ -0.231 log10(F10.7) -1.21 cos(SZA) \ +0.60 cos^2(SZA) +0.404 log10(IL_5) -7.21 \quad \text{(Eq 1)}$$

Figure 4 summarises the phase-inferred peak XL flux calculated from VLF phase perturbation levels using equation (1) compared with the NOAA measured peak flux for each of the flare events identified on the NPM - Scott Base path (blue circle with SD uncertainty ranges shown as blue error bars). Black vertical dashed lines indicate the lower flux thresholds for M- and X-class flares. A line of best fit is plotted (yellow line), along with an *x*=*y* line (dashed orange) that would be achieved with an exact match. The line of best fit and the *x*=*y* line agree very well. Also shown is the line of best fit determined by George et al. [2019] using the 10 X-class flares only, extrapolated into the M-class flare range (red line). This plot shows two things, firstly that the inclusion of the M-class flares has resulted in a best fit line that is closer to the x=y line than that generated by X-class flares only in George et al., and secondly, that it is appropriate to use VLF phase perturbations as a proxy for solar flare peak X-ray XL flux over a wide range of flux values.

In Table 1 uncertainty values are given in two ways. The first is the RMS uncertainty for the whole flare period as defined by the NOAA start and end times. The second is the standard deviation (SD) of the measured and inferred XL flux at the flare peak, which is a useful measure of the uncertainty in the flare classification [e.g., see George et al., 2019]. The earlier linear regression analysis of the 10 X-class flares on the N-S NPM to Scott Base path resulted in a MSE of 0.014 $(\log_{10}(Wm^{-2}))^2$ [George et al., 2019]. This can be expressed as an RMS value of 0.118 $\log_{10}(Wm^{-2})$. Including M-class flares in the linear regression analysis increases the number of flares sampled from 10 to 104, but also includes smaller phase perturbations, potentially introducing more uncertainty in the fits. The RMS uncertainty between the X-ray flux I_L and the flux calculated using the regression coefficients I_{Fit} is calculated in the following way:

$$\text{RMS uncertainty} = \text{SQRT}[\ \text{mean}(Log10(I_L) - Log10(I_{Fit}))^2]$$

The uncertainty results for the X-class flare dataset analysed in George et al. [2019] are compared against the M- and X-class flare values determined in this study via columns (a) and (b) of Table 1, respectively. Column (b) of Table 1 summarises the regression analysis coefficient values for the combined X- plus M-class flare dataset on the same NPM to Scott Base path as analysed in George et al., [2019]. RMS uncertainty in the flare flux increases by only about 10% compared with the previous X-class only analysis (since, from Table 1,

$10^{0.160}/10^{0.118} = 1.10$). However, Figure 4 shows that the best fit line for X and M-class flares lies closer to the idealised x=y line than the best fit line from George et al. [2019], suggesting that the inclusion of M–class flares in the regression analysis helps produce more realistic regression coefficients. The SD uncertainty of 0.138 $\log_{10}$(XL flux) for the NPM - Scott Base flares corresponds to a factor of $10^{0.138} = 1.37$ implying, for example, that a X1.5 flare would be within X1.1 to X2.1, which indicates reasonable accuracy. In comparison, the earlier rather simplistic error range estimate of uncertainty in George et al. [2019] reported a much larger range of an average flare in that study of M2.0 < X1.5 < X10.7. Table S3 in supplementary information provides a list of the uncertainty ranges for each flare analysed on the NPM – Scott Base path, using the linear regression coefficients to calculate the peak X-ray XL flux levels, and the NOAA flare start times.

The uncertainty values found for the N-S path using M- and X- class flares as shown in column (b) are taken as the baseline factor for the RMS and SD rows in our further analysis reported in the following sections. The baseline level being represented by (x1) in bold, i.e., a normalised to a factor of 1. In the next section the RMS and SD results for different paths, and different sets of regression parameters are compared to these baseline values, with the relative values given in parentheses in each column. Thus the relative values indicate the factor by which the values have changed compared to the baseline NPM to Scott Base path using the full set of regression parameters discussed in section 2.4.

3.2 NAA-SGO [using revised NOAA flare start times]

In this subsection the differences in undertaking linear regression analysis on solar flares that impact a long west-east path are investigated. The W-E NAA to SGO path that spans the North Atlantic from the eastern seaboard of the USA across to Finland is used. In all, 38 M- and 3 X-class flares met the selection criteria requiring whole-path illumination conditions (see section 2.2). The linear regression analysis results are summarised in column (c) of Table 1. Comparison with the M- and X- class flare results on the north-south path in column (b) shows that the regression coefficient for the phase perturbation parameter is larger by a factor of 11.6/6.7 = 1.7, which is similar to the ratio of the two paths lengths, i.e., 2.0. The IL_5 parameter coefficient value is similar to that found for the north-south path, while the other coefficients are noticeably different in magnitude or sign. The overall flare RMS, and peak flux SD uncertainties are larger for the W-E path than the N-S path, by factors of ~1.9 and ~2.2 respectively. Note that these ratios are similar to the ratio of the two path lengths. Table 1 includes the ratios of the uncertainty levels in each results box in the form, e.g., (x1.8) to indicate the value is 1.8 times larger

Figure 5 summarises the phase-inferred peak XL flux, calculated using the coefficients shown in column (c) of Table 1, compared with the NOAA measured peak flux, for each of the flare events identified on the W-E NAA to SGO path (blue circle with SD uncertainty ranges). As before a line of best fit to the data, and an $x=y$ line are plotted. It can be seen that the line of best fit shows reasonable agreement with the $x=y$ line, although slightly under-estimating the peak fluxes of the weaker flares, and over-estimating the stronger flares. The spread of the data points about the best fit line in Figure 5 is larger than that shown in Figure 4, which is consistent with the larger SD uncertainty value shown, i.e., 0.307 compared with 0.138. In practice this means that using the NAA to SGO phase data a X1.5 flare would be classified within M7.4 < X1.5 < X3.0 compared to the X1.1 < X1.5 < X2.1 range reported for the NPM to Scott Base data. In both Figure 5 and Figure 4 the best fit line crosses the x=y line at about the same flux level, i.e., at about X1, changing from slightly under-reporting M-class flares to slightly over-reporting X-class flares. The same behaviour is seen for the best fit line from George et al. [2019] shown in Figure 4, which suggests that such cross-over behaviour may be a feature of the VLF phase measurements and could be worthy of further study.

4. Operational technique [VLF phase start and end times]

So far in this study advantage has been taken of the availability of satellite-measured X-ray fluxes to identify the flare start and end times, as well as providing a measure of the XL flux just prior to the flare. In this section linear regression analysis between phase perturbation levels and measured XL flux during X- and M-class flare events is repeated, but this time with flare start and end times determined from VLF phase (see section 2.3), and with no inclusion of XL flux levels prior to flare start (IL_5) in the regression analysis. This effectively allows an estimate of solar flare XL X-ray flux levels using ground-based observations only (VLF phase, and F10.7 cm solar radio flux) independent of space based measurements. For comparison the same flare groups as in section 3 are used. As before, linear regression analysis is undertaken only on the flares which occur when the whole transmitter – receiver path is illuminated, with the condition SZA<80º imposed. However, operational identification of solar flare events using VLF phase would probably require additional checks to compensate for falsely ascribed perturbations. Improvements in the VLF results could come from more refined flare start and end time algorithms, although that is not the focus of this current study. One area of complexity in using VLF observations for flare timing analysis is due to a time delay by which the flare-induced electron density lags behind the flare flux, particularly in response to fast changing X-ray flux levels [Žigman et al., 2007]. The influence of this effect on start and end time determination was discussed in further detail in George et al. [2019].

Figure 6 shows four examples of the XL flux variations during solar flares. GOES XL fluxes are shown in orange, while the XL fluxes derived from VLF phase are shown in blue. Two flare examples from the N-S NPM to Scott Base path (an X-class and an M-class event) are provided in the left-hand panels. The plot begins at the start time of the flares determined from the VLF phase perturbation levels, and ends at the NOAA flare end time. The right-hand panels show X- and M-class flare examples on the W-E NAA to SGO path in the same format as the left-hand panels. These examples show that the VLF phase data can be used to reproduce the X-ray flux variations during the flare for both X and M-class flares – on both paths. At the start times of the flares shown in the figure, the VLF phase XL flux levels are typically higher than the GOES XL flux levels, and indicate that the VLF paths analysed here begin to respond to solar flare X-ray fluxes just below 10^{-5} Wm^{-2}, i.e., just below M1-class flares. This is a consequence of the equations produced by the regression analysis, where a 0 º phase perturbation leads to flux levels in the region of 10^{-5} Wm^{-2} using the coefficients given in Table 1 when in operational mode, i.e., columns (d) and (e). In the example given in Figure 6, the GOES fluxes are initially below this flux level, and only exceed it after some minutes. Because the pre-flare X-ray flux level is not set by the IL_5 satellite observations (in the case of the operational technique) there is potentially a discrepancy between the GOES and VLF phase-determined X-ray flux levels at the start of the flare. The variation of VLF phase-based XL flux matches closely to the GOES XL flux throughout the rest of each flare example.

The results of the linear regression analysis are given in column (d) of Table 1 for the N-S path, and column (e) for the W-E path. Column (d) shows the values found for the N-S NPM to Scott Base path without using satellite-provided X-ray fluxes but with ground-based determined start times. A small change in the scaling factor for $\Delta\varphi$ occurs relative to the

NOAA start and end timing analysis which included IL_5 in that case, i.e., relative to column (b), but the SZA terms remain essentially unchanged. The most notable difference is in the increase and change of sign in the coefficient for the solar F10.7 flux, suggesting that this parameter is compensating for the lack of IL_5 in describing the state of the D-region ionosphere prior to the flare event. Despite some changes in the linear regression coefficients when using flare start and end times based on VLF phase perturbation measurements, the RMS of the flare XL flux and the SD of the peak XL flux show little variation (x1.0 and x0.9, respectively) compared with the analysis done using NOAA start and end times plus IL_5 satellite observations.

In Table 1, column (e) shows the linear regression results for the W-E NAA to SGO path using ground-based observations only. Similar adjustments in the coefficients for $\Delta\varphi$ (decrease) and F10.7 flux (increase) are seen in the W-E NAA to SGO path results shown relative to column (c), the NOAA-based results. As with the N-S path, the flare XL flux RMS and peak XL flux SD show small improvements compared with the NOAA-based results, but their relative changes compared with the N-S path values in column (b) remain close to the ratio of the two path lengths, i.e., x1.8 and x1.7, respectively.

The peak XL flux calculated for each flare event analysed on the fully illuminated N-S path (upper panel) and the fully illuminated W-E path (lower panel) are shown in Figure 7 in the same format as Figures 4 and 5. The line of best fit for the flare events on the long N-S path matches the x=y line closely, indicating the potential for operational flare classification using ground-based observations alone. For the shorter W-E path, there is a slightly higher SD than for the longer path, and the line of best fit shows a somewhat increasing divergence at higher XL flux levels compared to the x=y line.

5. Discussion

The use of VLF phase measurements on a long subionospheric propagation path to infer solar flare X-ray (XL) flux levels has previously been shown to be more reliable than when using VLF amplitude measurements [George et al., 2019]. Here the VLF phase data from two different subionospheric propagation paths are analysed to identify the parameters that need to be taken into account when extending the technique to a wider range of transmitter – receiver combinations. However, in deploying a VLF receiver to undertake subionospheric observations it is often easier for researchers to monitor long West-East or East-West orientated paths rather than long North-South paths. This is due to the locations of existing VLF transmitters; for long N-S paths receiver locations become limited to South America, Africa, Antarctica, and some Southern Hemisphere islands. If one wishes a simpler long path dominated by sea water, and a high powered highly stable VLF transmitter, the options become even more limited, strongly favouring Antarctica. Long sea-dominated East-West or West-East paths open up many locations in the Northern Hemisphere which should be easier to deploy and operate in than Antarctic locations; hence, one of the reasons for considering them in the current study.

The two different time series of VLF transmitter phase measurements analysed here have the advantage of accumulating more than 10 years of data on each path, however only a small number (<10) of X-class flares occurred during daylight illumination conditions in each dataset. This provided a limited event sample with which to undertake linear regression analysis, and would be an obstacle to the use of new transmitter – receiver observational datasets for X-class flare analysis. However, extending the range of X-ray XL fluxes by a factor of 10, from just X-class to X- and M-class flares, increases the number of analysable flare events by about a factor of 10, but only results in an increase in the linear regression analysis RMS uncertainty by 10%.

Using different length subionospheric propagation paths to infer XL flux levels has a potentially larger effect on the RMS uncertainty levels. Two factors contribute to changes in RMS uncertainty levels, the geographical separation of the receiver from the transmitter, and the frequency of transmission. Shorter path lengths result in proportionally increased RMS uncertainty in the inferred XL flux levels. This interpretation is supported by the similarity between the factor of 1.7 decrease in path length between the NPM to Scott Base path and NAA to SGO, with the equivalent RMS uncertainty increase of a factor of 1.8-1.9 (see Table 1 values in parentheses). One reason for this increase in uncertainty is likely due to smaller phase perturbation levels on shorter paths, with a larger influence of any background noise. A second reason is due to more complex modal makeup on shorter paths as described by the mode theory of VLF propagation [Wait, 1961]. On long paths during daytime conditions there is likely to be only one dominant propagation mode (*n*=1, transverse magnetic). The response to solar flare-induced changes in the lower ionospheric boundary of the subionospheric waveguide will be well behaved in the presence of a single propagation mode. However for shorter paths, more modes will exist, with varying attenuation rate responses to the changing lower ionospheric boundary conditions during a flare [Wait and Spies, 1964; Rhoads and Garner, 1967].

Additional potential difficulties in comparing different path responses to solar flares are likely to occur for E-W or W-E propagation [Crombie, 1958], and for high- versus low-latitude paths [Thomson et al., 2005, 2018, 2020]. Asymmetric attenuation in the Earth-ionosphere waveguide is introduced by the Earth's magnetic field because propagation in directions inclined to the Earth’s horizontal field are non-reciprocal. This results in azimuthally dependent attenuation. VLF waves exhibit larger attenuation when propagating westward than when propagating eastward [e.g., Crombie, 1958; Hutchins et al., 2013], potentially reducing the phase perturbation response to solar flares, thereby increasing the uncertainty level in derived XL flux. Additional factors such as land conductivity or land/sea conductivity boundaries [Westerlund et al., 1969; Thomson 1985] can introduce significant mode conversion, making the propagation response to solar flares more complex and therefore more uncertain, leading to likely increases in the RMS and SD over the all sea paths studied here.

This study has shown here that it is possible to estimate XL flux from ground-based observations alone, effectively providing an operational technique that is independent of satellite measurements and complementary to them. VLF phase perturbations can be used to determine the flare occurrence, in combination with the F10.7 cm UV index to compensate for day-to-day variations in background ionospheric conditions. Analysis shows that the RMS uncertainties are unchanged or slightly improved compared with the results determined when including satellite observations. Similar results are found for the flare peak flux estimates. Typical flare classification SD uncertainties of XL flux, with or without, satellite-included techniques can be summarised as about ±0.14 $\log_{10}(Wm^{-2})$ for subionospheric paths of ~10,000 km and frequency ranges of 20-25 kHz. This uncertainty in the log10(flux) is equivalent to an uncertainty of a factor of $10^{0.14}$ or about 1.4 in the flux or the flare magnitude, e.g., an derived M5 flare would have an error range of ~M3.6 to M6.9. SD uncertainties in the determination of peak flux levels proportionally increase for shorter path lengths, with about ±0.3 $\log_{10}(Wm^{-2})$ for subionospheric paths of ~5,000 km. Note that these statements apply to subionospheric propagation paths that are primarily all-sea paths, and could be substantially different for more complex over-land paths which can exhibit substantial variations in surface conductivity levels from region to region [Ferguson and Snyder, 1990].

Although an approximate proportionality of path length change is seen in the linear regression coefficient for the phase perturbation parameter, the same simple relationship is not evident in the other coefficients in Table 1, i.e., F10.7, SZA, and IL_{5}. For the satellite-included regression analysis the coefficients changed by typical factors of 0.3 – 2, and changed sign, when comparing the long N-S path with the shorter W-E path. However, for the ground-based regression analysis (i.e., not including the IL_5 parameter) the coefficients changed by typical factors of 2 – 4 but without changing sign, when comparing the two paths. The delicate balance exhibited between the regression analysis parameter coefficients makes it difficult to predict these coefficient values when converting from a known path to an unknown one.

6. Conclusions

Using linear regression analysis of solar flare effects on two different subionospheric VLF phase datasets, both covering more than 10 years of observations, the following is found:

1.) Extending previous analysis on a long N-S path to include M-class flares as well as X-class flares increases the root mean square (RMS) uncertainty of the derived XL flux over the duration of the flare by ~10%.

2.) Uncertainty in the derived XL flux at the flare peak on the long N-S path has a standard deviation (SD) of ±0.138 $Log_{10}Wm^{-2}$, allowing reasonable discrimination between the classification of M and X-class flares.

3.) Good agreement is found between the peak XL flux derived for M- and X- class flares and those measured by GOES.

4.) The regression analyses on our two paths (NPM-Scott Base, NAA-SGO) show that the RMS and SD uncertainties increase by a factor of ~2, in inverse proportion to the lengths of the paths.

5.) Investigations were made of a limited set of ‘operational’ parameters to derive XL fluxes. No increases in RMS or SD uncertainty levels were introduced by the removal of satellite-based regression parameters such as IL_{5}, the XL flux level measured prior to the flare onset.

The techniques proposed in this study support the idea of independent monitoring M- and X-class flare X-ray flux levels from entirely ground-based measurements. To provide global measurements of solar flare flux, observations of VLF phase perturbations on multiple transmitter-receiver paths will be required. The results determined by this study provide insight into the likely errors and uncertainties that each path would contribute to such networks.

Acknowledgements: The authors would like to thank AntarcticaNZ for providing support for the VLF observations made at Arrival Heights through event K060, NOAA for providing the GOES X-ray flux data, and Canadian Natural Research Council the solar UV, F10.7 cm flux. The authors would also like to thank Anna Tarr of Otago University for archiving the corrected VLF NPM phase and amplitude data for each of the flare events, which can be found at: https://zenodo.org/record/4774464. GOES X-ray flux data can be found at: https://satdat.ngdc.noaa.gov/sem/goes/data/. F10.7 measurements are provided courtesy of the Canadian National Research Council (NRC) and Canadian Space Agency (CSA), and can be found at: https://www.spaceweather.gc.ca/forecast-prevision/solar-solaire/solarflux/sx-5-en.php. The authors would like to thank Paul Muir of Otago University for his assistance with Figure 1. MAC would like to acknowledge support from the UK Research and Innovation (UKRI-NERC) through National Capability Space Weather Observatory funding (NC-SS SWO).

References

Berdermann, J., Kriegel, M., Banyś, D., Heymann, F., Hoque, M. M., Wilken, V., et al. (2018). Ionospheric response to the X9.3 Flare on 6 September 2017 and its implication for navigation services over Europe. Space Weather, 16, 1604– 1615. https://doi.org/10.1029/2018SW001933

Blanc P. and L. Wald, The SG2 algorithm for a fast and accurate computation of the position of the sun for multi-decadal time period. Solar Energy 88, 3072-3083, 2012, doi: 10.1016/j.solener.2012.07.018

Cannon, P., et al. (2013). Extreme space weather: Impact on engineered systems and infrastructure. Summary Report, Royal Academy of Engineering, London, URL: https://www.raeng.org.uk/publications/reports/space-weather-summary-report

Clilverd, M. A., et al. (2009), Remote sensing space weather events: The AARDDVARK network. Space Weather, 7, S04001, doi:10.1029/2008SW000412

Clilverd, M. A., Duthie, R., Rodger, C. J., Hardman, R. L. & Yearby, K. (2017). Long-term climate change in the D-region. Sci. Rep., 7:16683, doi:10.1038/s41598-017-16891-4

Clilverd, M. A., Rodger, C. J., van de Kamp, M. & Verronen, P. T. (2020). Electron precipitation from the outer radiation belt during the St Patrick's Day storm 2015: observations, modelling, and validation. J. Geophys. Res., 125, e2019JA027725, doi:10.1029/2019JA027725

Cresswell-Moorcock, K., Rodger, C. J., Clilverd, M. A., & Milling, D. K. (2015). Techniques to determine the quiet day curve for a long period of subionospheric VLF observations. Radio Sci., 50, 453–468, https://doi.org/10.1002/2015RS005652

Crombie, D. D. (1958). Differences between east-west and west-east propagation of VLFsignals over long distances. J. Atmospheric and Terrest. Phys., 12(2-3), 110-117, https://doi.org/10.1016/0021-9169(58)90081-3

European Union Avian Safety Agency (2021). Safety Information Bulletin: Effects of Space Weather on Aviation. EASA SIB No.: 2012-09R1, Issued: 28 April 2021

Ferguson, J. A., & Snyder, F. P. (1990). Computer programs for assessment of long wavelength radio communications, version 1.0: Full FORTRAN code user's guide. (Naval Ocean Systems Center Tech. Doc. 1773, DTIC AD-B144 839). Alexandria, 853 VA: Defense Technical Information Center

George, H. E., Rodger, C. J., Clilverd, M. A., Cresswell - Moorcock, K., Brundell, J. B., & Thomson, N. R. (2019). Developing a Nowcasting Capability for X - Class Solar Flares

Using VLF Radiowave Propagation Changes. Space Weather, 17, 1783– 1799. https://doi.org/10.1029/2019SW002297

Georgoulis, M. (2012). On Our Ability to Predict Major Solar Flares. Astrophys. Space Sci. Proc. 30, 93-116, https://doi.org/10.1007/978-3-642-29417-4

Hargreaves, J. K. (1992).The solar-terrestrial environment. Cambridge: Cambridge University Press. https://doi.org/10.1017/CBO9780511628924

Hutchins, M. L., Jacobson, A. R., Holzworth, R. H., & Brundell, J. B. (2013). Azimuthal dependence of VLF propagation. J. Geophys. Res., 118, 5808– 5812, doi:10.1002/jgra.50533

ICAO (2018). Manual on Space Weather Information in Support of International Air Navigation, International Civil Aviation Organization Doc 10100, 2018. Available from: https://www.icao.int/airnavigation/METP/Panel%20Documents/Doc.10100.Space%20Weather%20Manual%20FINAL%20DRAFT%20Version.pdf

Knipp, D. J., & M. Hapgood (2019), Space weather aviation forecasting on a global scale, Eos, 100, https://doi.org/10.1029/2019EO135277

Knipp, D. J., et al. (2016), The May 1967 great storm and radio disruption event: Extreme space weather and extraordinary responses, Space Weather, 14, 614– 633, doi:10.1002/2016SW001423

Kolarski, A., & Grubor, D. (2014). Sensing the Earth's low ionosphere during solar flares using VLF signals and goes solar X-ray data. Adv. SpaceRes. 53, 1595–1602, https://doi.org/10.1016/j.asr.2014.02.022

Kontogiannis, I., Georgoulis, M. K., Park, S-H. & Guerra, J. A. (2018). Testing and Improving a Set of Morphological Predictors of Flaring Activity. Solar Phys., 293:96, https://doi.org/10.1007/s11207-018-1317-2

Kusano, K., Iju, T., Bamba, Y., & Inoue, S. (2020) A physics-based method that can predict imminent large solar flares. Science 369(6503):587–591. https://doi.org/10.1126/science.aaz2511

Lotz, S. I. & Clilverd, M. A. (2019). Demonstrating the Use of a Class of Min-Max Smoothers for D Region Event Detection in Narrow Band VLF Phase. Radio Science, 54, 233–244, https://doi.org/10.1029/2018RS006701

Marqué, C., et al. (2018). Solar radio emission as a disturbance of aeronautical radionavigation. J. Space Weather Space Climate, 8, https://doi.org/10.1051/swsc/2018029

McRae, W. M., & Thomson, N. R. (2000). VLF phase and amplitude: daytime ionospheric parameters. J. Atmos. Sol.-Terr. Phys., 62(7), 609-618, https://doi.org/10.1016/S1364-6826(00)00027-4

McRae, W. M., & Thomson, N. R. (2004). Solar flare induced ionospheric D-region enhancements from VLF phase and amplitude observations. J. Atmos. Sol.-Terr. Phys., 66(1), 77-87, https://doi.org/10.1016/j.jastp.2003.09.009

Mitra, A. P. (1974). Ionospheric Effects of Solar Flares, Springer Netherlands, ISBN 9789027704672, doi: https://doi.org/10.1007/978-94-010-2231-6

Redmon, R. J., Seaton, D. B., Steenburgh, R., He, J., & Rodriguez, J. V. (2018). September 2017's geoeffective space weather and impacts to Caribbean radio communications during hurricane response. Space Weather, 16, 1190–1201. https://doi.org/10.1029/2018SW001897

Rhoads, F.J. & Garner, W.E. (1967). An investigation of the modal interference of VLF radio waves. Radio Sci., 2(6), 539-546, https://doi.org/10.1002/rds196726539

Rodger, C. J., Enell, C.-F., Turunen, E., Clilverd, M. A., Thomson, N. R., & Verronen, P. T. (2007). Lightning-driven inner radiation belt energy deposition into the atmosphere: implications for ionisation-levels and neutral chemistry. Ann. Geophys., 25, 1745–1757, https://doi.org/10.5194/angeo-25-1745-2007

Sato, H., Jakowski, N., Berdermann, J., Jiricka, K., Heßelbarth, A., Banyś, D., & Wilken, V. (2019). Solar radio burst events on 6 September 2017 and its impact on GNSS signal frequencies. Space Weather, 17, 816– 826. https://doi.org/10.1029/2019SW002198

Thomson, N. R. (1985). Reflection of VLF radio waves from distant mountain ranges. J. Geophys. Res., 47, 353–362, https://doi.org/10.1016/0021-9169(85)90015-7

Thomson, N. R., Clilverd, M. A., Brundell, J. B., & Rodger, C. J. (2021). Quiet night Arctic ionospheric D region characteristics. Journal of Geophysical Research: Space Physics, 126, e2020JA029043. https://doi.org/10.1029/2020JA029043

Thomson, N. R., Rodger, C. J., & Clilverd, M. A. (2005). Large solar flares and their ionospheric D region enhancements. J. Geophys. Res., 110, A06306, https://doi.org/10.1029/2005JA011008

Thomson, N. R., Rodger, C. J., & Dowden, R. L. (2004). Ionosphere gives size of greatest solar flare. Geophys. Res. Lett., 31, L06803, https://doi.org/10.1029/2003GL019345

Veronig, A., Temmer, M., Hanslmeier, A., Otruba, W., & Messerotti, M. (2002). Temporal aspects and frequency distributions of solar soft X-ray flares. Astronomy and Astrophysics, v.382, p.1070-1080, https://doi.org/10.1051/0004-6361:20011694

Wait, J. R. (1961). A New Approach to the Mode Theory of VLF Propagation. J. Research NBS, 65D1-101, 37-46, https://doi.org/10.6028/JRES.065D.007

Wait, J.R., & Spies, K.P. (1964). Characteristics of the Earth-ionosphere waveguide for VLF radio waves. NBS Tech. Note 300, Natl. Bur. of Stand., Boulder, Colo. https://www.govinfo.gov/app/details/GOVPUB-C13-1fc83a916d87542f34917847f89b9f0b

Wenzel, D., Jakowski, N., Berdermann, J., Mayer, C., Valladares, C., & Heber, B. (2016). Global ionospheric flare detection system (GIFDS). Journal of Atmospheric and Solar-Terrestrial Physics, 138–139, 233-242, https://doi.org/10.1016/j.jastp.2015.12.011

Westerlund, S., F., Reder, H., & Abom, C. (1969). Effects of polar cap absorption events on VLF transmissions. Planet. Space Sci., 17, 1329–1374, https://doi.org/10.1016/0032-0633(69)90203-7

Žigman, V., Grubor, D., & Šulić, D. (2007). D-region electron density evaluated from VLF amplitude time delay during X-ray solar flares. Journal of Atmospheric and Solar-Terrestrial Physics, 69, 775-792 https://doi.org/10.1016/j.jastp.2007.01.012

Samuel R. G. Belcher, James B. Brundell, Sophie Cook, Craig J. Rodger, and Neil R. Thomson, Department of Physics, University of Otago, P.O. Box 56, Dunedin, New Zealand. (email: belsa476@student.otago.ac.nz, james.brundell@otago.ac.nz, cooso287@student.otago.ac.nz, craig.rodger@otago.ac.nz, neil.thomson@otago.ac.nz).

Mark A. Clilverd, British Antarctic Survey (UKRI-NERC), High Cross, Madingley Road, Cambridge CB3 0ET, England, U.K. (e-mail: macl@bas.ac.uk).

Tero Raita, Sodankylä Geophysical Observatory, University of Oulu, 955 Sodankylä, Finland. (email: tero.raita@sgo.fi)

Tables

Table 1. The linear region coefficients, and the uncertainty results for the X-class flare dataset analysed in George et al. [2019] are compared against the combined X- and M-class flare values determined in this study for N-S and W-E paths.

Description	**(a)** George et al., 2019	**(b)** Figure 4 Equation 1 Table S1	**(c)** Figure 5 Table S2	**(d)** Figure 7 (upper panel)	**(e)** Figure 7 (lower panel**)**
Path orientation	N-S	N-S	W-E	N-S	W-E
Path illumination	Mid-point	Full	Full	Full	Full
Flare start time detection	NOAA	NOAA	NOAA	VLF phase	VLF phase
No.of flares and type	X=10	M=98, X=6	M=38, X=3	M=98, X=6	M=38, X=3
Path length (km)	11,246	11,246	5,667	11,246	5,667
Regression Coefficients for each measured parameter					
for Phase perturbation	6.5×10^{-3}	6.7×10^{-3}	11.6×10^{-3}	6.3×10^{-3}	9.3×10^{-3}
for F10.7	-0.423	-0.231	0.245	0.576	1.367
for Cos(SZA)	-2.64	-1.21	0.63	-1.13	-2.338
for Cos^2(SZA)	1.97	0.60	-1.21	0.48	1.772
for IL_5	0.698	0.404	0.437	-------	-------
Constant	-9.03	-7.21	2.25	6.51	22.81
Uncertainty					
RMS ($log_{10}Wm^{-2}$)	0.118	0.160 **(x1)**	0.296 (x1.9)	0.158 (x1.0)	0.289 (x1.8)
SD at peak flux ($log_{10}Wm^{-2}$)	--------	0.138 **(x1)**	0.307 (x2.2)	0.130 (x0.9)	0.231 (x1.7)

Figures

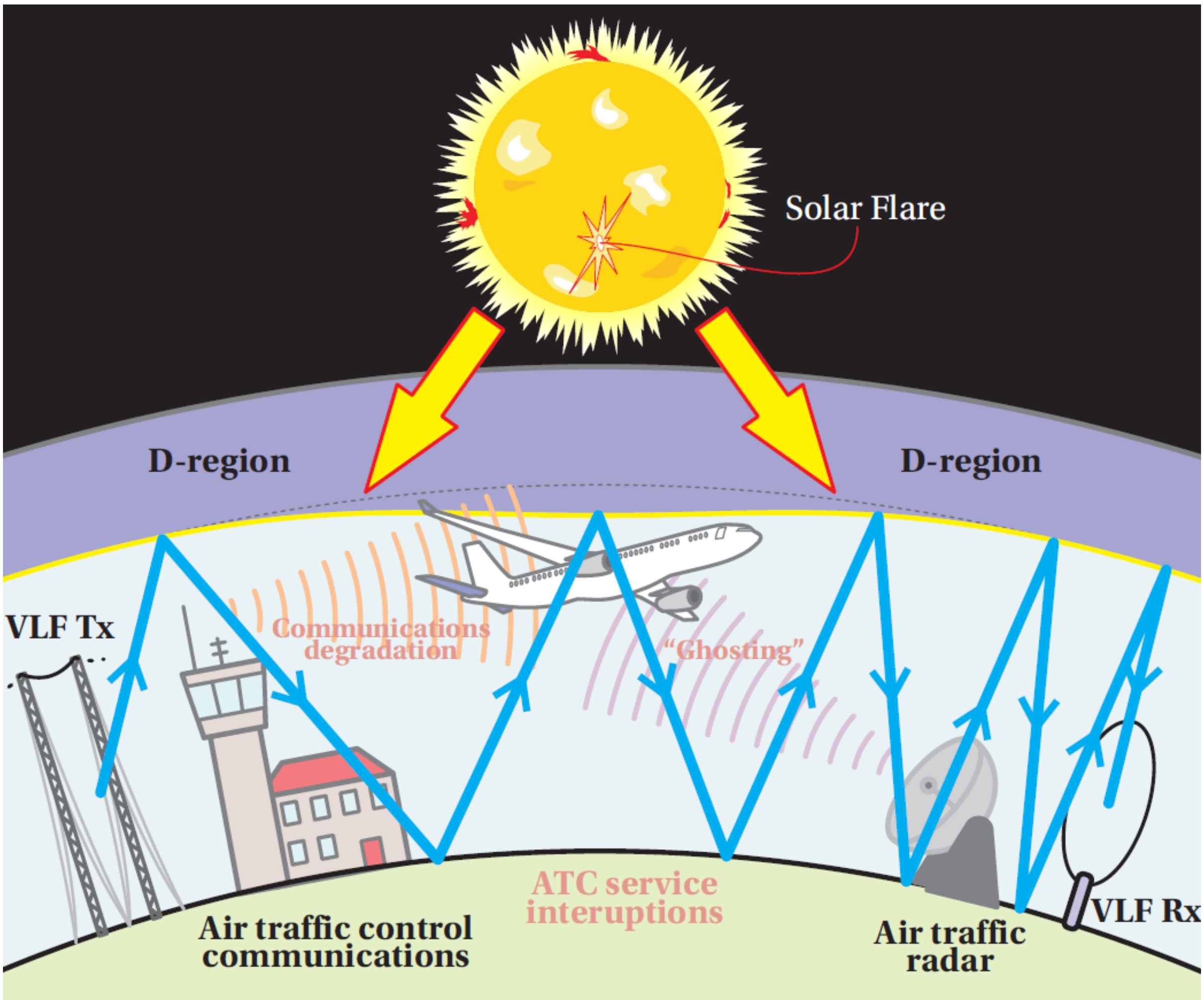

Figure 1: A schematic that illustrates the systems impacted by solar flare effects on the ionospheric D-region, namely VLF subionospheric signal propagation, along with air traffic radar systems and air-traffic control (ATC) communication systems. Communication degradation, and radar ghosting can lead to ATC service interruptions. .

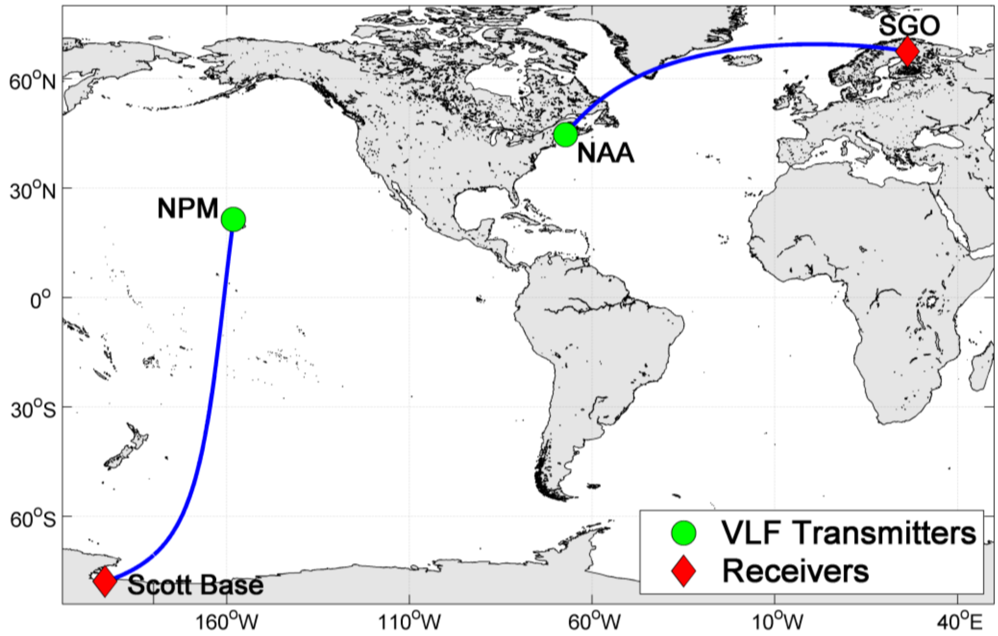

Figure 2. Map showing the subionospheric VLF great circle paths used in this study (blue lines). VLF Transmitters are shown as green dots, while the VLF receivers are shown as red diamonds. The largely north-south (NS) path is from NPM to Scott Base, while the largely West-East path is from NAA to the Sodankylä Geophysical Observatory (SGO).

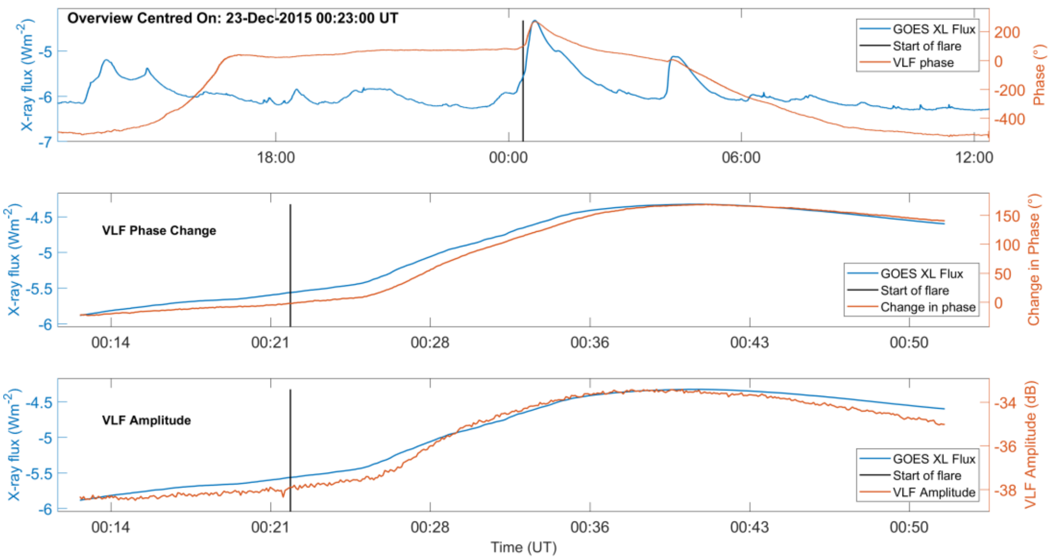

Figure 3. VLF data from NPM - Scott Base observed on 22-23 December 2015. Upper panel. The VLF phase variation over 24 hours (orange) centered on the flare event compared with GOES XL X-ray fluxes over the same period (blue). An M-class flare peaked at 00:40 UT, with a vertical black line indicating its NOAA-determined onset time of 00:23 UT. Middle panel. The variation of VLF phase perturbations (orange) and XL flux (blue) during the time period around the flare event. Lower panel. The variation of VLF amplitude (orange) and XL flux (blue) during the time period around the flare event.

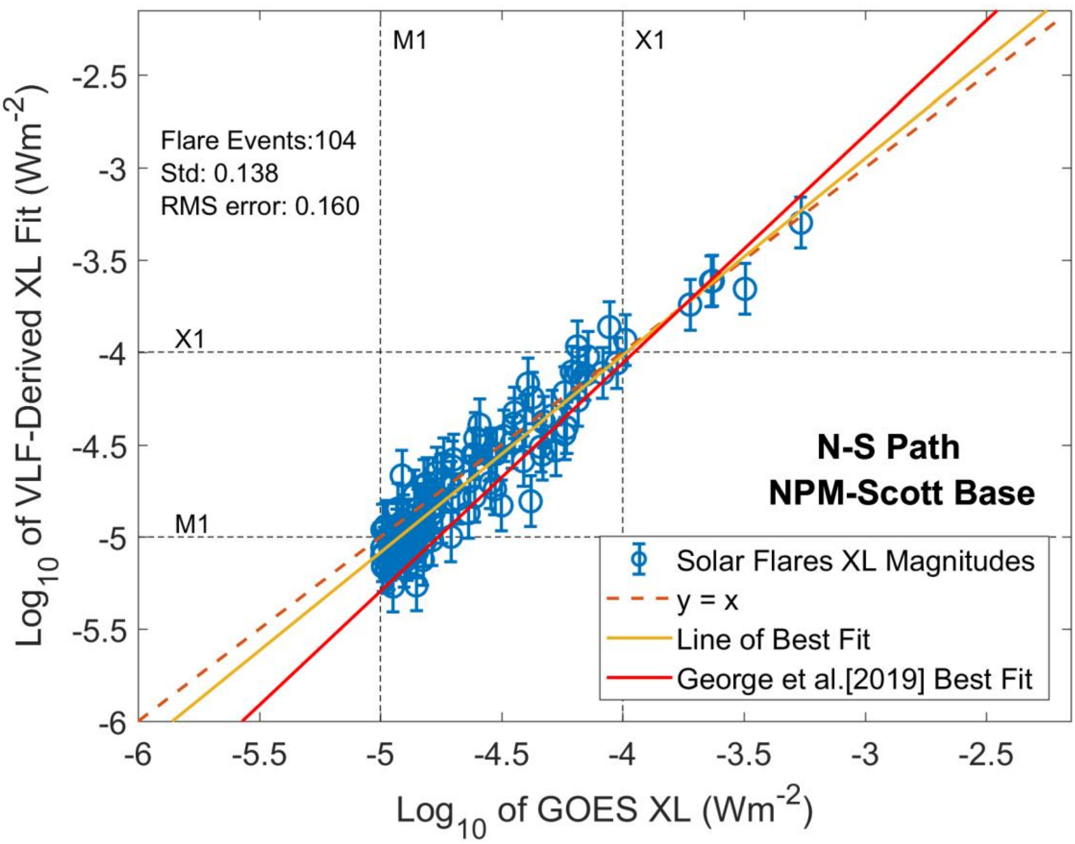

Figure 4. Comparison between the GOES measured XL peak solar flare fluxes with those derived from the subionospheric VLF data (blue circles), with error bars shown by the blue vertical lines. This example is for the NPM to Scott Base N-S path, using the NOAA determined flare start times. The orange dashed line shows a *y*=x relationship, while the mustard coloured line shows the best fit straight line between these two parameters for the 104 flares plotted. For contrast, the red line is the best fit straight line relationship for the 10 X-class development solar flares with the data taken from *George et al.* [2019].

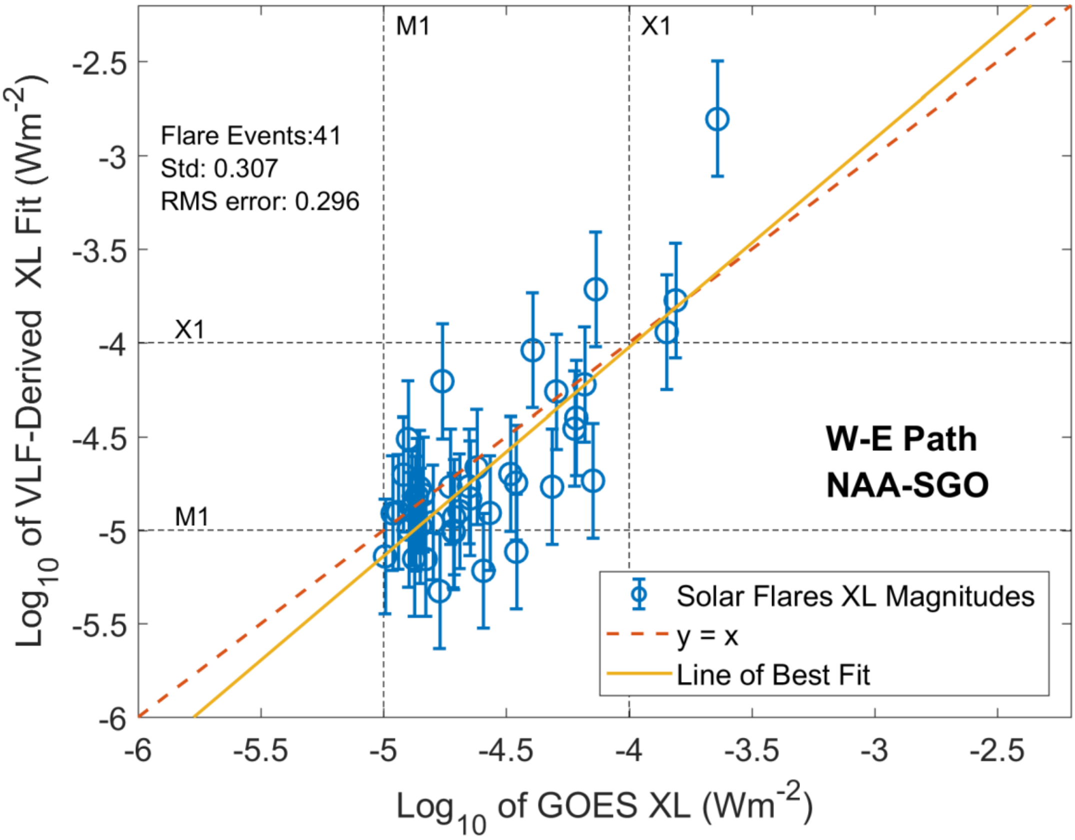

Figure 5. As figure 4, but flares occurring on the largely W-E path from NAA to the Sodankylä Geophysical Observatory (SGO). Once again NOAA-determined start times are used, and the line of best fit is shown for the 41 flares.

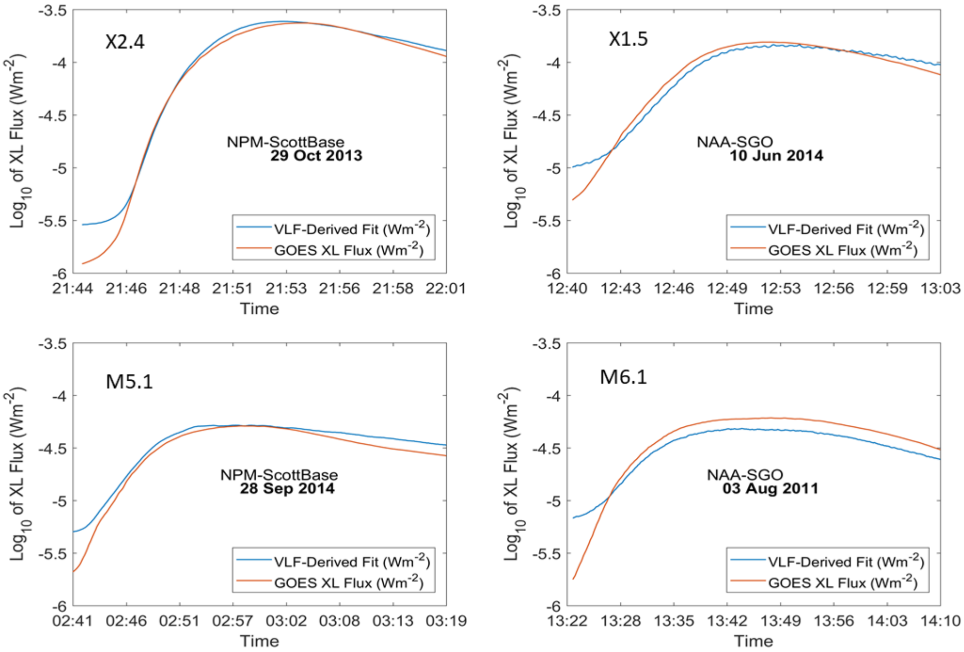

Figure 6. Examples of the time variation between VLF-derived X-ray fluxes and those measured by the GOES satellite when only ground-based observations are used. The data shown is from the VLF phase-determined start time. Note the left-hand panels are for the N-S NPM to Scott Base path, and the right-hand panels for the W-E NAA to SGO path. Flare classification is indicated in each panel.

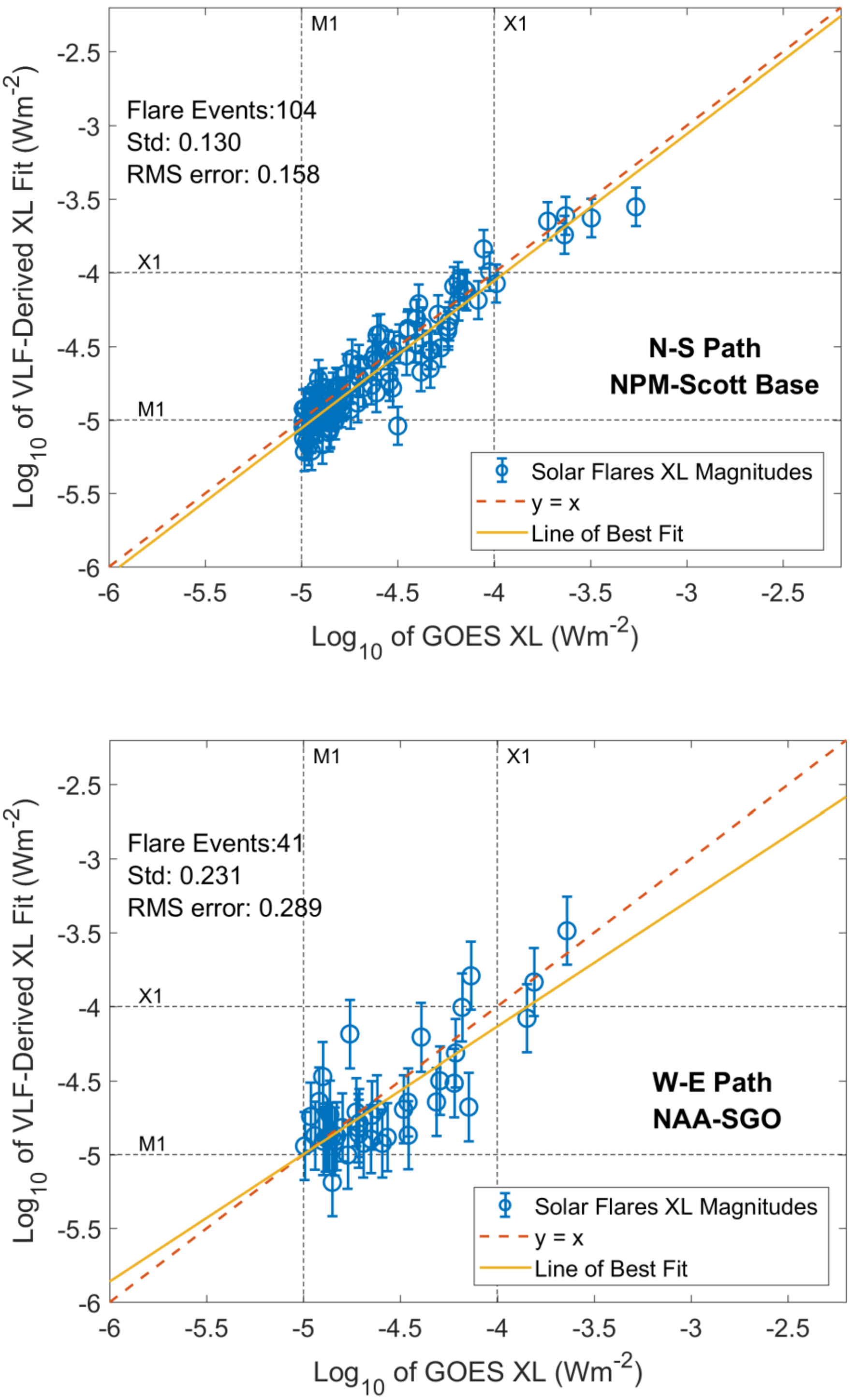

Figure 7. Comparison of the VLF ground based peak X-ray flux magnitudes without any satellite data involved (i.e., using VLF phase start times) against the GOES satellite measurements, in the same format as Figure 4. The upper panel is for the N-S path from NPM to Scott Base, and the lower panel the W-E path from NAA to SGO.

Figure 1.

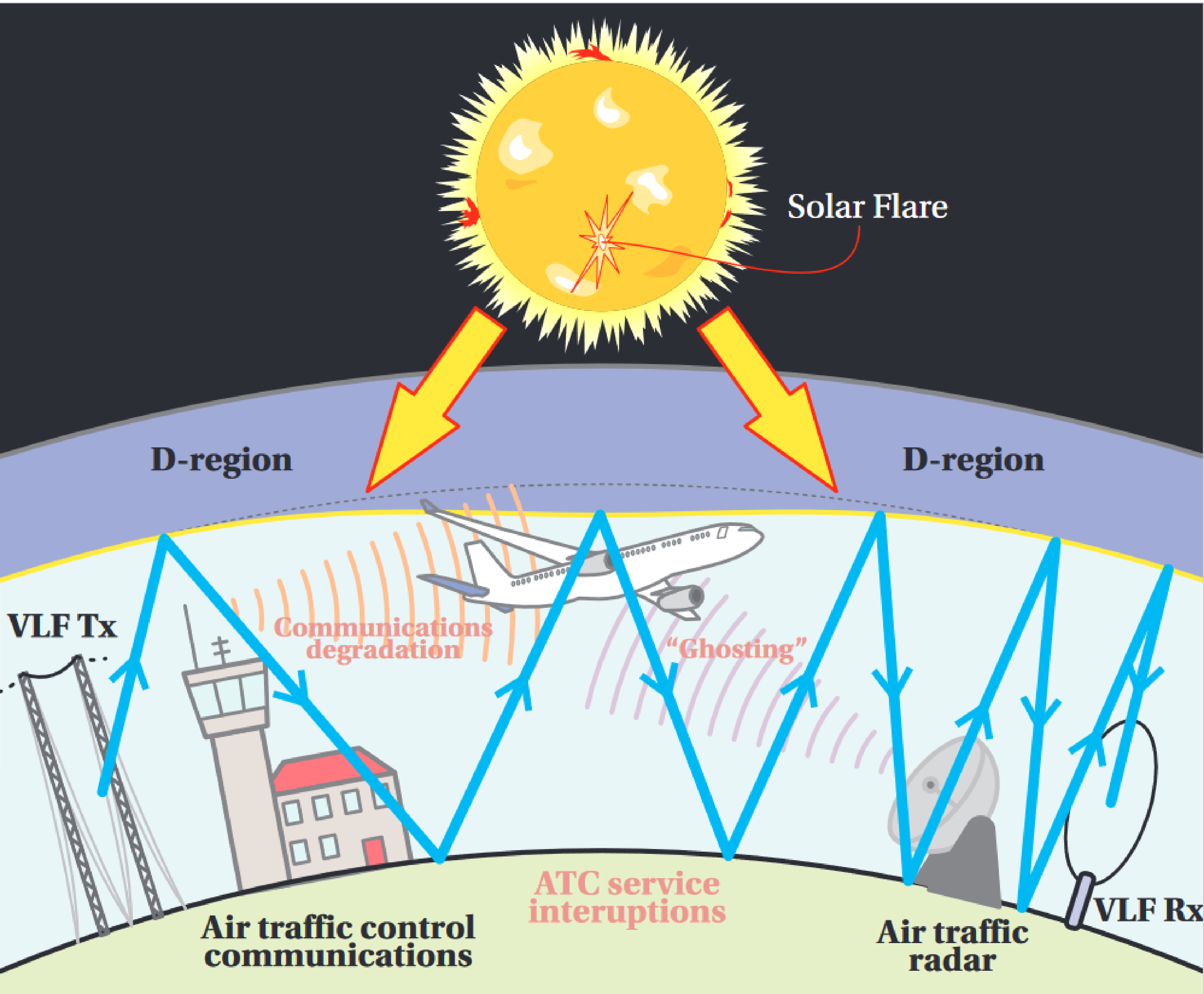
Solar Flare
D-region
D-region
VLF Tx
Communications degradation
"Ghosting"
ATC service interuptions
Air traffic control communications
Air traffic radar
VLF Rx

Figure 2.

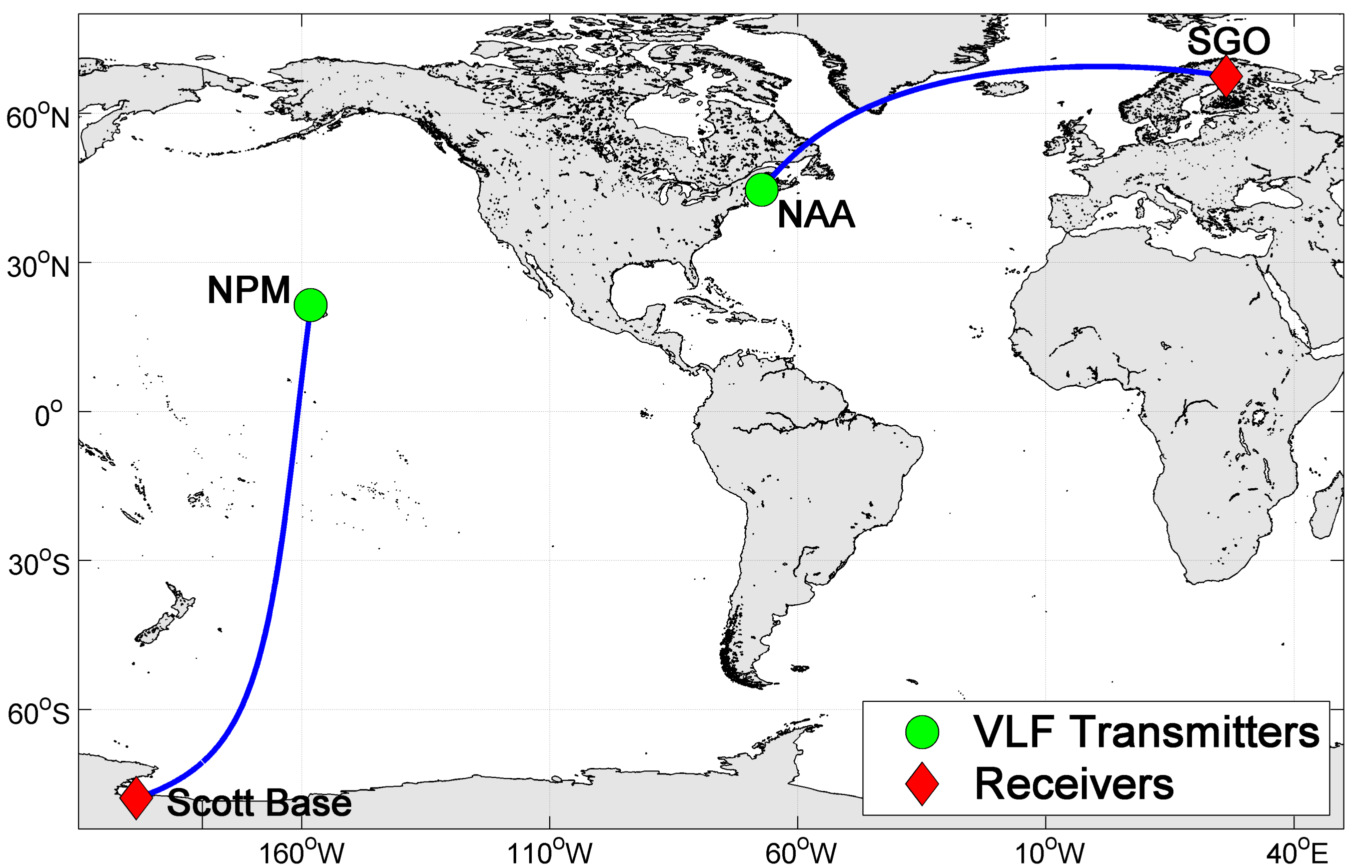

SGO
NAA
NPM
Scott Base
VLF Transmitters
Receivers
60°N
30°N
0°
30°S
60°S
160°W
110°W
60°W
10°W
40°E

Figure 3.

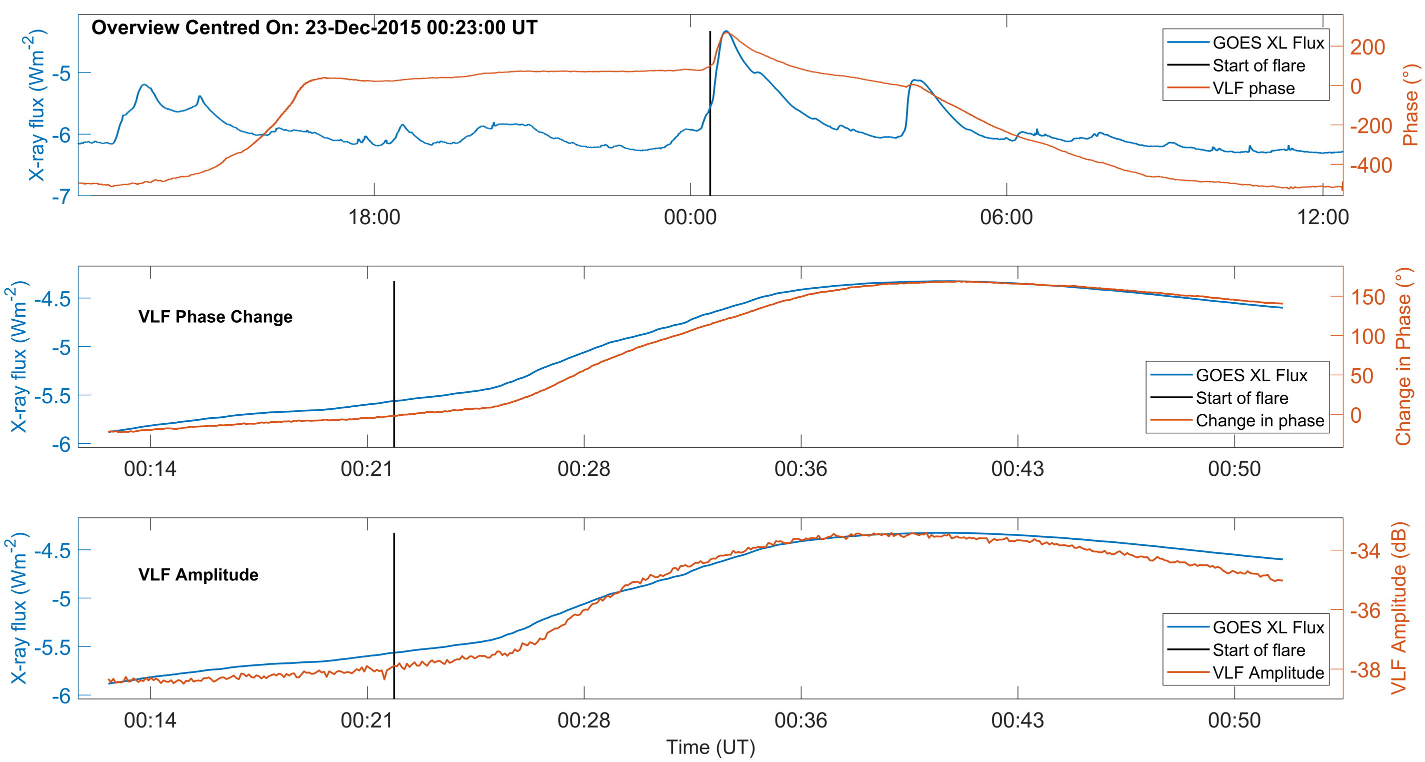

Overview Centred On: 23-Dec-2015 00:23:00 UT
X-ray flux (Wm^{-2})
Phase (°)
GOES XL Flux
Start of flare
VLF phase
-5
-6
-7
200
0
-200
-400
18:00
00:00
06:00
12:00
VLF Phase Change
X-ray flux (Wm^{-2})
Change in Phase (°)
GOES XL Flux
Start of flare
Change in phase
-4.5
-5
-5.5
-6
150
100
50
0
00:14
00:21
00:28
00:36
00:43
00:50
VLF Amplitude
X-ray flux (Wm^{-2})
VLF Amplitude (dB)
GOES XL Flux
Start of flare
VLF Amplitude
-4.5
-5
-5.5
-6
-34
-36
-38
00:14
00:21
00:28
00:36
00:43
00:50
Time (UT)

Figure 4.

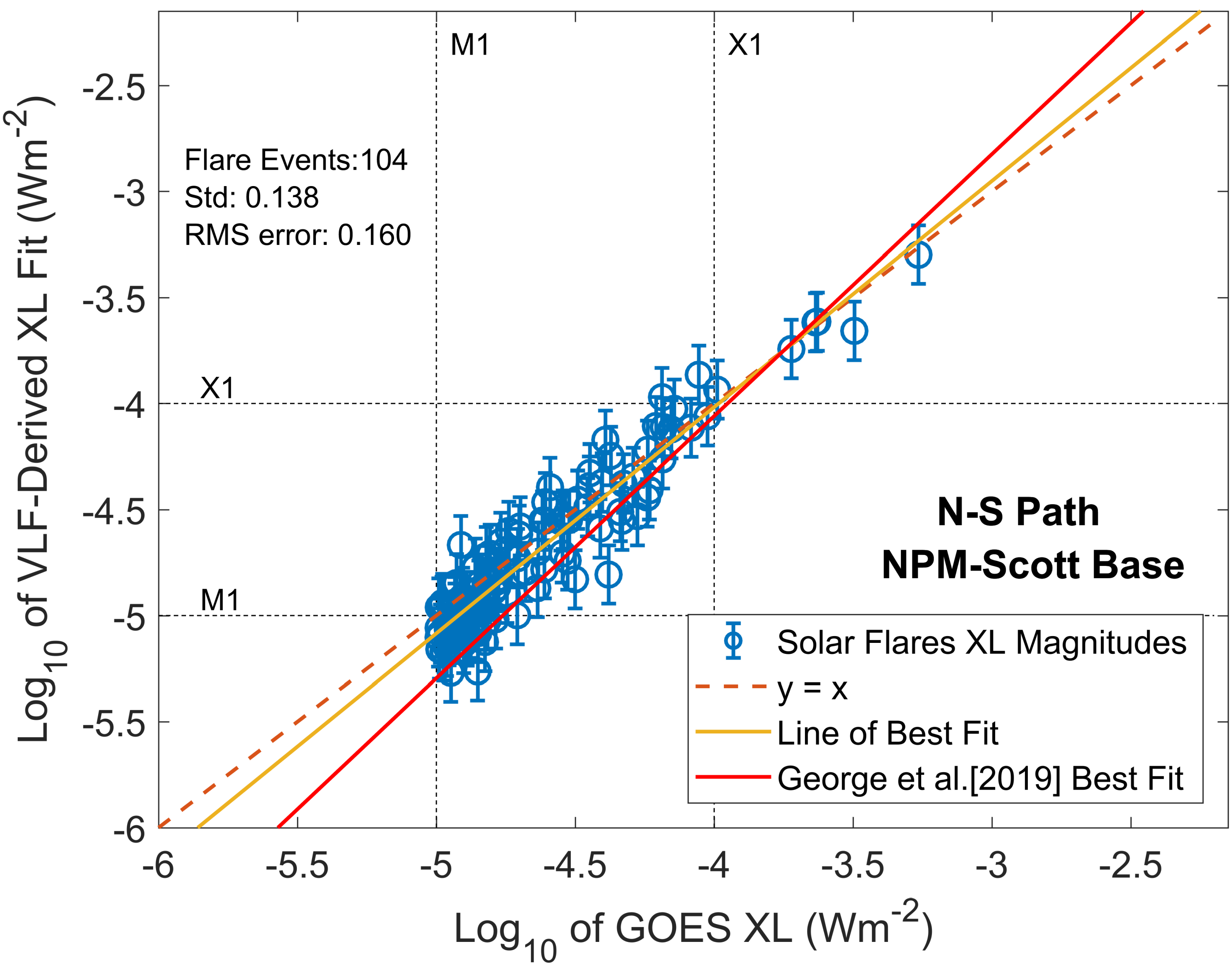

M1
X1
Flare Events:104
Std: 0.138
RMS error: 0.160
X1
M1
N-S Path
NPM-Scott Base
Solar Flares XL Magnitudes
y = x
Line of Best Fit
George et al.[2019] Best Fit
Log10 of VLF-Derived XL Fit (Wm-2)
Log10 of GOES XL (Wm-2)
-2.5
-3
-3.5
-4
-4.5
-5
-5.5
-6
-6
-5.5
-5
-4.5
-4
-3.5
-3
-2.5

Figure 5.

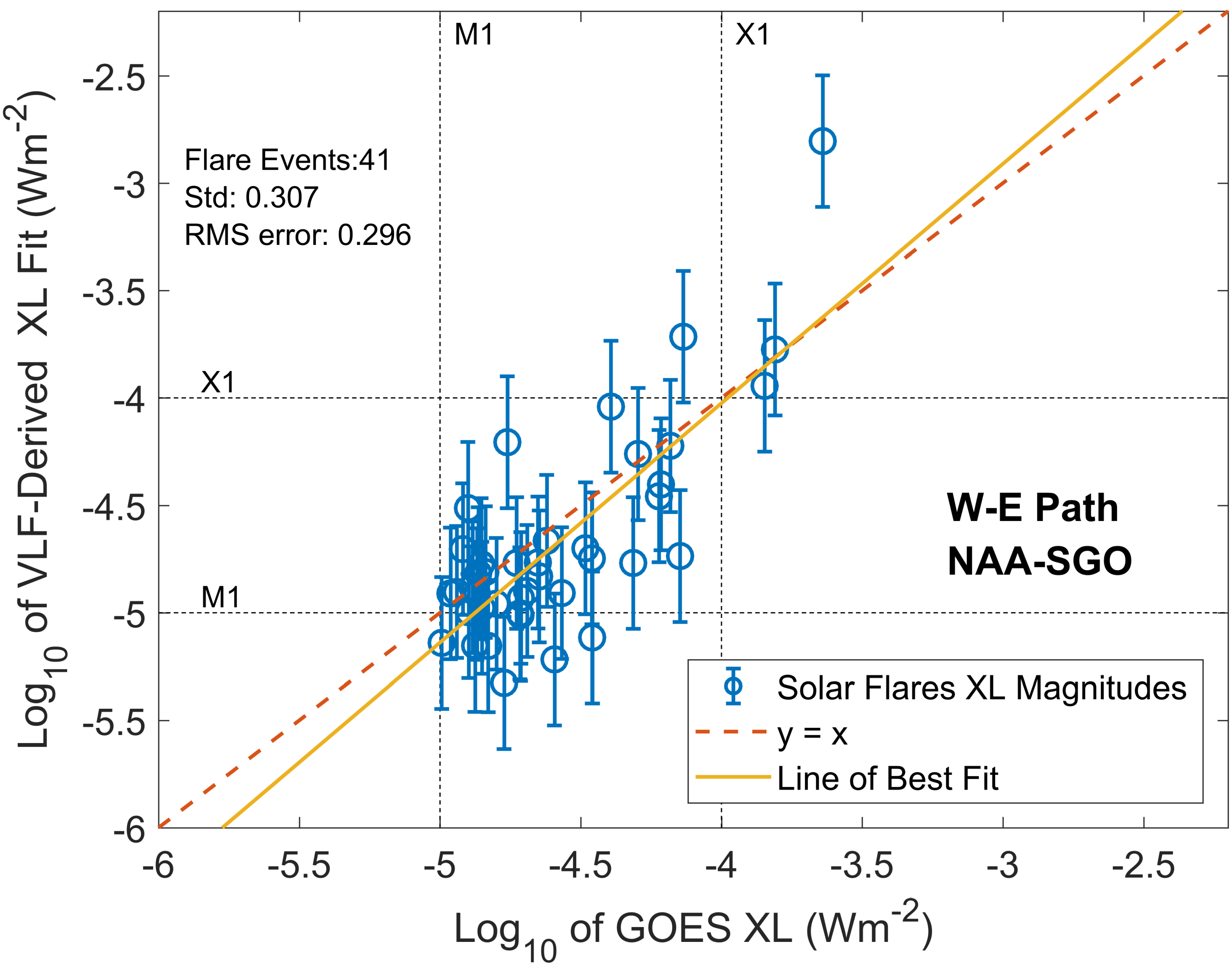
M1
X1
Flare Events:41
Std: 0.307
RMS error: 0.296
W-E Path
NAA-SGO
Solar Flares XL Magnitudes
y = x
Line of Best Fit
-2.5
-3
-3.5
-4
-4.5
-5
-5.5
-6
Log10 of VLF-Derived XL Fit (Wm-2)
Log10 of GOES XL (Wm-2)

Figure 6.

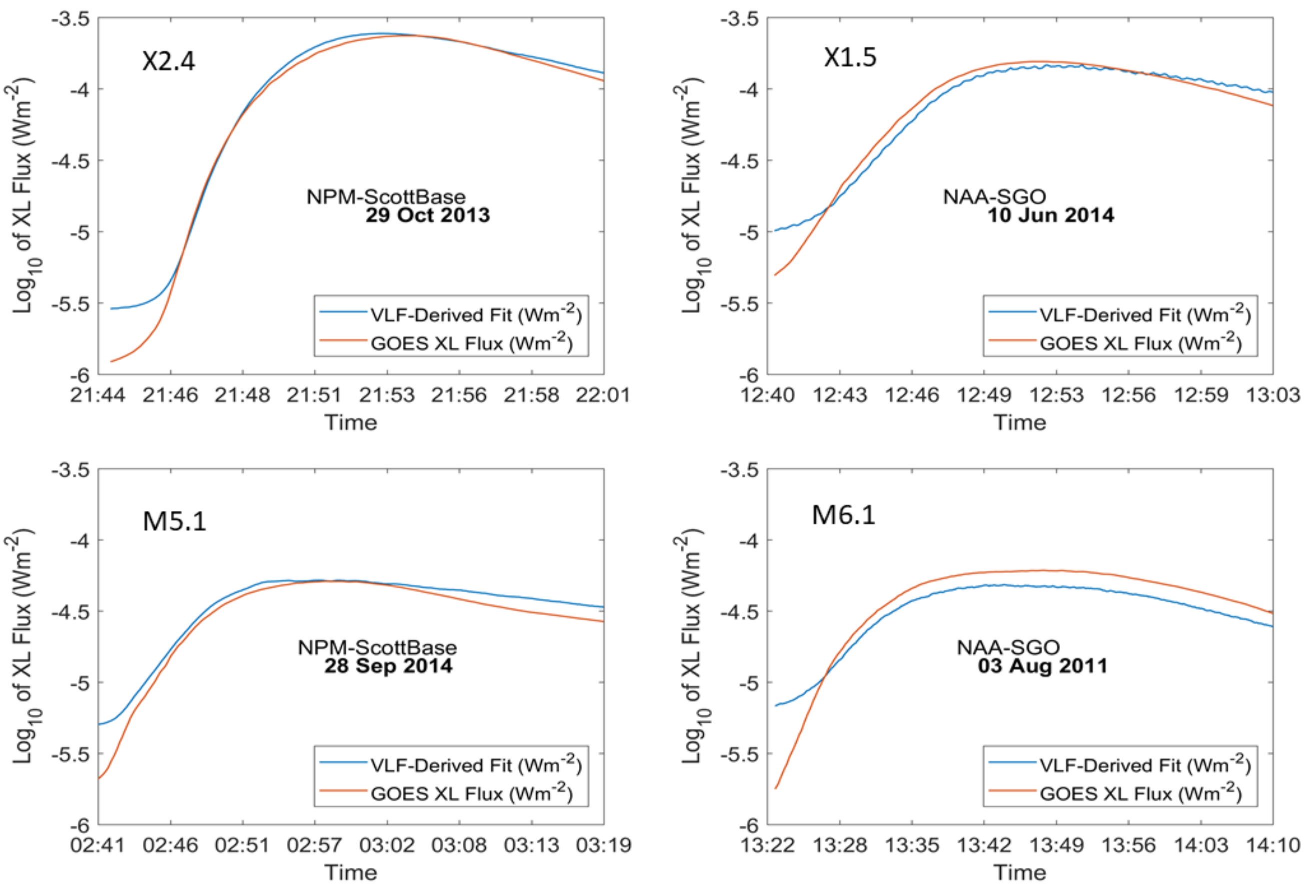
X2.4
NPM-ScottBase
29 Oct 2013
X1.5
NAA-SGO
10 Jun 2014
M5.1
NPM-ScottBase
28 Sep 2014
M6.1
NAA-SGO
03 Aug 2011
VLF-Derived Fit (Wm-2)
GOES XL Flux (Wm-2)
Log10 of XL Flux (Wm-2)
Time

Figure 7.

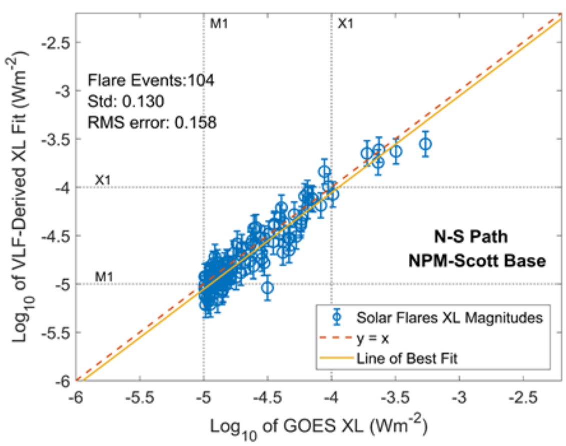
Flare Events:104
Std: 0.130
RMS error: 0.158
N-S Path
NPM-Scott Base
Solar Flares XL Magnitudes
y = x
Line of Best Fit
M1
X1
Log10 of VLF-Derived XL Fit (Wm-2)
Log10 of GOES XL (Wm-2)

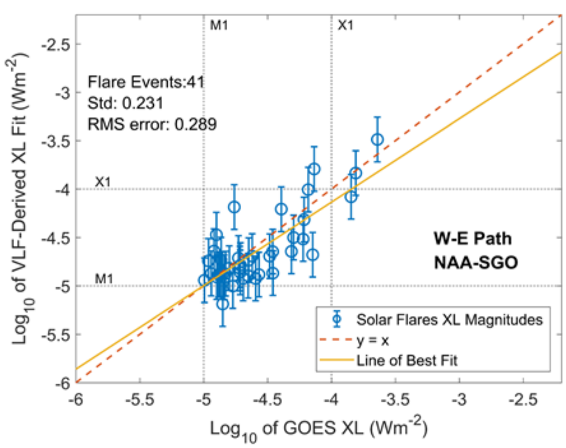
Flare Events:41
Std: 0.231
RMS error: 0.289
W-E Path
NAA-SGO
Solar Flares XL Magnitudes
y = x
Line of Best Fit
M1
X1
Log10 of VLF-Derived XL Fit (Wm-2)
Log10 of GOES XL (Wm-2)